Computed Structure of Low Strain Rate Partially Premixed CH_4/Air Counterflow Flames: Implications for NO Formation

LINDA G. BLEVINS* and JAY P. GORE

Thermal Sciences and Propulsion Center, 1003 Chaffee Hall, School of Mechanical Engineering, Purdue University, West Lafayette, IN 47907-1003, USA

Results from computations of low strain rate, partially premixed methane/air counterflow flames are reported. The Oppdif computer code was used with GRI-Mech 2.11 to obtain the results. When the fuel-side equivalence ratio (Φ_B) is above 2.5, the present flame structure can be described as a CH_4/air premixed flame merged with a CO/H_2/air nonpremixed flame. When Φ_B is below 2.5, the two flame zones exist on opposite sides of the stagnation plane, and the CO/H_2/air nonpremixed flame is characterized by hydrocarbon concentration peaks on its fuel-side edge. Broad NO destruction regions, caused primarily by CH_i + NO reactions, exist between the resulting double hydrocarbon concentration peaks. The fuel-side equivalence ratio is the most important indicator of how rapidly NO is destroyed relative to how rapidly it is formed, and NO destruction reactions are more important in pure diffusion flames than in partially premixed flames for the present low strain rate computations.

INTRODUCTION

Industrial flames are typically categorized as nonpremixed (diffusion) flames when the fuel and air are introduced into the combustor in separate streams. However, many of these initially nonpremixed flame systems are more accurately described as being partially premixed. For example, based on flame appearance and local species measurements, a previous experimental study revealed that initially nonpremixed natural gas/air swirl flames confined in a quartz radiant heating tube burned in partially premixed mode [1]. Partial premixing exists when a portion of the combustion air mixes with the fuel prior to burning, resulting in locally fuel-rich and/or fuel-lean mixtures surrounded by air. This scenario results in a gradient of the local fuel-to-air ratio. Partially premixed burning may also occur in practical systems initially categorized as premixed systems, such as certain gas turbine combustors, when the fuel/air mixing is not entirely uniform [2]. Some other examples of partial premixing are lifted flames in furnaces, domestic appliance flames, and burning in the region of pyrolysis and mixing in fires.

Experimental research in laboratory flames demonstrates that partial premixing results in either a double flame [3–6] or a triple flame [7–12], depending on the fuel and air flow arrangement. The double flame exists at the interface between counterflowing streams, with one stream consisting of a rich fuel/air mixture and the other of air [3–5]. A double flame consists of (1) a premixed flame formed in the fuel-rich mixture, and (2) a nonpremixed flame formed between the products of this rich, premixed flame and the opposing air stream. A variation of the counterflow double flame was stabilized at the interface between a lean fuel/air mixture and a pure fuel layer [6]. Another type of double flame is that of a coflow (Bunsen-type) burner, which consists of a rich fuel/air jet with a surrounding, parallel flowing air stream. The Bunsen flame is referred to here as a double flame because it is commonly believed that this type of flame consists of an inner rich premixed flame cone and an outer diffusion flame cone [13]. The triple or tribrachial flame propagates through the mixing layer formed between adjacent fuel and air streams in a direction perpendicular to the fuel concentration gradient [12]. The leading tip of the flame is the connecting point for three trailing flame zones: (1) a rich premixed flame extending toward the fuel layer, (2) a lean premixed flame extending toward the air layer, and (3) a trailing nonpremixed flame extending along the line of

*Corresponding author. Present address: National Institute of Standards and Technology, Building and Fire Research Laboratory, Bldg. 224, Room B360, Gaithersburg, MD 20899-0001. E-mail: linda.blevins@nist.gov

0010-2180/99/$–see front matter
PII S0010-2180(98)00059-5

Published by Elsevier Science Inc.

stoichiometric fuel/air mixture. In most practical devices, the combustion process is not well enough understood to determine if double or triple flames or some other structures exist locally. Consequently, the factors affecting pollutant formation and destruction in practical flames which exhibit partial premixing are far from being completely understood.

Recent laboratory studies demonstrated that partially premixed burning can affect exhaust nitrogen oxide (NO_x) emissions from flames either favorably or unfavorably relative to nonpremixed burning [14–16]. The exhaust NO_x emission index ($EINO_x$, g/kg fuel) from laminar, coflow, methane/air flames was found to decrease to a minimum value and then increase as air was incrementally added to the fuel jet [14]. An analysis based on the trends in global residence time and temperature in these flames revealed that the nonmonotonic $EINO_x$ trend can not be predicted from the traditional understanding of thermal NO formation in either purely premixed or completely nonpremixed flames [16]. Similar $EINO_x$ behavior has been reported for laminar, coflow, partially premixed ethane/air flames [15], for turbulent, coflow, partially premixed natural gas/air flames [16], and for counterflow, partially premixed CH_4/air flames [17]. Various other exhaust NO_x trends have been reported for partially premixed turbulent flames [18–20]. Motivated by the practical importance of partial premixing and by the unresolved reasons for the exhaust $EINO_x$ behavior of partially premixed laboratory flames, a computational study was undertaken with the aim of elucidating the factors that affect NO formation within partially premixed flames. The results of this study are reported in the present paper.

Smyth recently published a study of NO formation in a Wolfhard-Parker CH_4/air diffusion flame [21]. This study was based on a comprehensive experimental database collected over several years which included measurements of velocity obtained with laser Doppler velocimetry (LDV), temperature obtained with a fine wire, radiation-corrected thermocouple, quantitative NO and OH concentrations obtained with laser-induced fluorescence (LIF), relative O atom and CH concentrations obtained with LIF, relative H atom and CH_3 concentrations obtained with multiphoton ionization (MPI), and CH_2 concentrations derived from these data. Smyth combined these data to generate reaction rate profiles for some of the chemical reactions that form and consume NO. Even with the comprehensive set of experimental data described above, Smyth concluded that the relative contributions of different routes for NO production could not be assessed without measuring additional species profiles (such as HCN). Thus, because of the extensive amount of data required, and the experimental challenges associated with obtaining these data, computations presently provide the most detailed way to analyze NO chemistry in flames. It is recognized that detailed kinetics computations provide their own set of challenges because there are uncertainties in the chemical kinetic rates that are available for combustion chemistry. The most recent realization of a methane combustion mechanism with NO chemistry is GRI-Mech 2.11, which was optimized and validated using experimental combustion data collected in a variety of flow reactors, low-pressure flames, and stirred reactors, with the goal of providing a reliable, standardized research and design tool [22]. GRI-Mech 2.11 was used in the present work.

The computations presented in this paper were performed for a simplified type of partially premixed flame, the laminar, counterflow flame established between a rich fuel/air stream and an opposing air stream. It is realized that the complex features of turbulent, partially premixed flames in practical combustors will not be captured with the present simplified analysis. Nonetheless, these computational results identify some features of partially premixed flame structure that affect NO formation and destruction, and that will hopefully generate new ideas for controlling NO formation in more practical flames.

The centerline fluid mechanics of a counterflow flame can be modeled using a similarity solution [23–27]. Early modeling studies of counterflow flames involved placing a potential flow, stagnation point source at an infinite distance from a compressible boundary layer [23,24]. This formulation resulted in flame solutions that could be characterized by a single characteristic strain rate defined as the potential flow

velocity gradient. An improved counterflow similarity solution which allows a finite separation distance between inlet nozzles and a locally varying velocity gradient (strain rate) is employed in the present work [25–27].

Using the improved similarity solution, Nishioka et al. computed the structure of partially premixed, methane/air counterflow flames [28]. The authors used a nozzle separation distance of 1.5 cm and varied the equivalence ratio of the rich fuel/air mixture between 1.5 and infinity (called the "pure diffusion flame" in the present paper). The partially premixed flames exhibited double flame structure. The majority of their work was performed for relatively high nozzle exit velocities (16 cm/s), resulting in high strain rates. They compared NO production rate profiles in the partially premixed flames with those from normal premixed and pure diffusion flames and concluded that there are two zones where NO is formed or consumed in high strain rate partially premixed flames. First, near the temperature peak or nonpremixed combustion region of a double flame, thermal NO formation takes place. Second, near the "premixed" combustion region of a double flame, Fenimore NO formation occurs on the air side and Fenimore NO destruction occurs on the fuel side. These authors also performed a limited number of calculations for low-velocity (5 cm/s, i.e. low strain rate) flames.

There has been at least one previous study focused on low strain rate, partially premixed, counterflow flames. Dupont et al. computed the structure of these flames using the improved similarity solution [29]. The authors used a nozzle separation distance of 6 cm with fuel side equivalence ratios of 1.6, 1.9, and infinity (pure diffusion flame). They found an unexpected central CH radical concentration peak between the two flame zones of the double flame for the operating conditions with strain rates of 10 s^{-1} to 20 s^{-1}. They found this type of behavior both when using the GRI-Mech 2.11 chemical mechanism [22] and when using the Miller-Bowman chemical mechanism [30].

Tanoff et al. published a study of the computed structure of partially premixed, CH_4/air counterflow flames [31]. These authors used a nozzle separation of 1.27 cm with fuel side equivalence ratios in the range of 1.3 to infinity (pure diffusion flame). They studied flames with high strain rates (100 s^{-1} to 900 s^{-1}), and did not find the intermediate hydrocarbon concentration peak. Thus, the higher strain rate computations of Nishioka et al. and Tanoff et al. did not result in the double hydrocarbon concentration peaks found in the lower strain rate work of Dupont et al. Understanding flames with both high and low strain rates is important because both regions exist in the laboratory jet flames for which the $EINO_x$ minimum was measured [32]. The goals of the present research were to elucidate factors affecting NO formation in computed low strain rate counterflow flames in order to complement previous higher strain rate work, and to provide a more complete understanding of the NO behavior in multi–strain rate partially premixed flames.

While the work of Dupont et al. involved imposing low strain by using a large separation distance of 6 cm between the fuel and air nozzles, the present work entails an alternate method. The objectives of this paper are (1) to report that a unique flame structure similar to that found by Dupont and her coauthors is also found for the present low strain rate flames, and (2) to explore the implications of the unique structure for NO formation and destruction in partially premixed flames.

OPPDIF COMPUTATIONAL METHOD

The Sandia National Laboratories code Oppdif [27] was combined with the GRI-Mech 2.11 reaction mechanism [22] to solve for velocity, temperature, and species concentrations along the centerline of partially premixed counterflow flames. The GRI-Mech 2.11 scheme contains 279 elementary reactions involving 49 chemical species. A schematic of the flame is shown in Fig. 1. In this configuration, a rich mixture of methane (CH_4) and air with equivalence ratio Φ_B is injected through one nozzle while air is injected through the other. The fuel side equivalence ratio, Φ_B, is defined as the fuel to air ratio of the mixture entering through the fuel nozzle divided by the stoichiometric fuel to air ratio (0.058 for CH_4). Combustion reactions take place on one or both sides of the stagnation

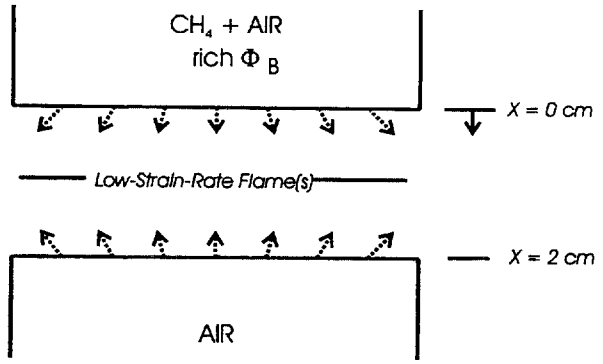

Fig. 1. Schematic of counterflow burner configuration.

plane in the present flames depending on the operating conditions.

Details of the Oppdif similarity solution are provided by Lutz and Kee [27] and are summarized here. The full equations that describe the flow are the axisymmetric continuity, momentum, energy, and species equations. The velocity in the axial or x direction is denoted as u (cm/s), and the velocity in the radial or r direction is denoted as v (cm/s). The two assumptions of the similarity solution are: (1) the axial velocity, temperature, species concentrations, and fluid properties vary only with distance along the axis, and (2) the radial velocity varies linearly with distance along the radius with a proportionality constant that varies only with axial distance. Based on these assumptions, a similarity variable, G (g/cm^3 · s), is defined as a function of x, where ρ (g/cm^3) is the fluid density:

$$G(x) = -\frac{\rho v}{r}. \tag{1}$$

The eigenvalue (H, dyne/cm^4) associated with the radial and axial momentum equations is defined in the following way, where p (dyne/cm^2) is the pressure:

$$H = \frac{1}{r}\frac{\partial p}{\partial r} = \text{const.} \tag{2}$$

If the variable $F(x)$ (g/cm^2 · s) is defined as:

$$F(x) = \frac{\rho u}{2}, \tag{3}$$

then the continuity, momentum, energy, and species equations become:

$$G(x) = \frac{d}{dx}\left(\frac{\rho u}{2}\right), \tag{4}$$

$$H - 2\frac{d}{dx}\left(\frac{FG}{\rho}\right) + \frac{3G^2}{\rho} + \frac{d}{dx}\left[\mu\frac{d}{dx}\left(\frac{G}{\rho}\right)\right] = 0, \tag{5}$$

$$\rho u\frac{dT}{dx} - \frac{1}{c_p}\frac{d}{dx}\left(\lambda_{con}\frac{dT}{dx}\right) + \frac{\rho}{c_p}\sum_k c_{pk}Y_kV_k\frac{dT}{dx} + \frac{1}{c_p}\sum_k h_k\dot{\omega}_k = 0, \tag{6}$$

and

$$\rho u\frac{dY_k}{dx} + \frac{d}{dx}(\rho Y_kV_k) - \dot{\omega}_kW_k = 0 \qquad k = 1, K. \tag{7}$$

Here, μ is the dynamic viscosity (g/cm · s), T is the temperature (K), c_p is the constant pressure specific heat of the mixture (erg/g · K), λ_{con} is the thermal conductivity of the mixture (erg/cm · K · s), c_{pk} is the constant pressure specific heat of the kth component of the mixture (erg/g · K · s), Y_k is the mass fraction of species k, V_k is the diffusion velocity of component k (cm/s, see Eq. 8 below), h_k is the enthalpy of formation of species k (erg/g), and $\dot{\omega}_k$ is the mass production rate of species k (g/cm^3 · s). The diffusion velocities V_k used in the above equations are defined using a mixture-averaged formulation,

$$V_k = -\frac{1}{X_k}D_{km}\frac{dX_k}{dx}, \quad \text{where}$$

$$D_{km} = \frac{1 - Y_k}{\sum_{j\neq k}^{K} X_j/D_{kj}}. \tag{8}$$

In these equations, X_k is the mole fraction of species k, D_{km} is the diffusion coefficient for species k in the mixture (essentially an "effective binary diffusivity" for k), D_{kj} is the diffusion coefficient of the pair k-j in a binary mixture, and K is the total number of species in the mixture (49 for GRI-Mech 2.11). A correction term is added to each diffusion velocity

such that the net species diffusion flux is zero [33, 34].

The boundary conditions include a flux condition imposed to account for diffusion into the convective stream at the nozzles,

$$x = 0: \quad F = \frac{\rho_0 u_0}{2}, \; G = -\rho_0 \left(\frac{v}{r}\right)_0, \; T = T_0, \tag{9}$$

$$x = L: \quad F = \frac{\rho_L u_L}{2}, \; G = -\rho_L \left(\frac{v}{r}\right)_L, \; T = T_L, \tag{10}$$

$$x = 0: \quad \rho u Y_k + \rho Y_k V_k = (\rho u Y_k)_0, \tag{11}$$

and

$$x = L: \quad \rho u Y_k + \rho Y_k V_k = (\rho u Y_k)_L. \tag{12}$$

Species diffusion into the nozzles is allowed. In the present study the fuel stream at $x = 0$ consists of fuel and air, while the oxidizer stream at $x = L$ consists of air only. Thermal species diffusion, radiation heat transfer, and buoyancy are neglected in the present analysis.

The above equations and boundary conditions constitute a one-dimensional boundary value problem with F, G, T, and Y_k as dependent variables. The kinetic rates and transport properties are found using the Sandia National Laboratories Chemkin II and Transport utility programs [33, 35]. The equations are discretized using finite differencing techniques. Diffusive terms are represented using central differencing, and convective terms are written as upwind differences. Oppdif features a hybrid Newton/time-integration procedure similar to the one described by Grcar et al [36].

During execution of Oppdif, the initial solution was found using an assumed temperature profile, and the energy equation was solved during subsequent iterations. Absolute convergence criteria for Newton iteration and for time stepping were both 1×10^{-6}. The initial grid contained nine evenly spaced points but was automatically adjusted by Oppdif and ultimately included about 125 points for each solution. The solutions yielded the same temperature behavior for different grid sizes, and thus were shown to be grid-independent. Oppdif was executed on an IBM RISC 6000 computer, and the run times often amounted to several hours. The best way to minimize computational time and increase chances of convergence was to find an initial converged solution and use that as the initial guess for a subsequent run in which the fuel side equivalence ratio was incrementally changed.

The method recommended by Takeno and Nishioka [37] for computing the NO_x emission index in counterflow flames is used in the present paper. The NO_x emission index is written as the ratio of the mass formation rate of NO_x per unit flame area to the mass consumption rate of fuel per unit area,

$$\mathrm{EINO}_x = \frac{\displaystyle\int_0^L \mathrm{MW}_{\mathrm{NO}_x} \dot{\omega}_{\mathrm{NO}_x} \, dx}{\displaystyle -\int_0^L \mathrm{MW}_{\mathrm{CH}_4} \dot{\omega}_{\mathrm{CH}_4} \, dx}. \tag{13}$$

Using a common method of assuming all of the NO exists as NO_2 for purposes of computing the NO emission index, the molecular weight of NO_2 is used for the entire calculation, and the resulting formula is used to compute the emission index:

$$\mathrm{EINO}_x = \frac{\displaystyle -2 \int_0^L G(x)(X_{\mathrm{NO}} + X_{\mathrm{NO}_2}) \frac{\mathrm{MW}_{\mathrm{NO}_2}}{\mathrm{MW}_{\mathrm{mix}}} \, dx}{\displaystyle 2F_{x=0} X_{\mathrm{CH}_4, x=0} \left(\frac{\mathrm{MW}_{\mathrm{CH}_4}}{\mathrm{MW}_{\mathrm{mix},x=0}}\right) + 2 \int_0^L G(x) X_{\mathrm{CH}_4} \left(\frac{\mathrm{MW}_{\mathrm{CH}_4}}{\mathrm{MW}_{\mathrm{mix}}}\right) dx}. \tag{14}$$

In this equation, X represents mole fraction and MW_{mix} is the molecular weight of the mixture. The first term in the denominator represents the total amount of fuel injected and the second term (a negative number) represents the total amount of fuel that bypasses the flame.

SELECTION OF OPERATING CONDITIONS

The strain rate in counterflow flames is defined as the radial velocity gradient tangential to the flame surface [38], while Oppdif yields axial velocity profiles in the direction perpendicular to the flame surface. The axial velocity gradient perpendicular to the flame surface scales with the radial velocity gradient tangential to the flame surface through the continuity equation. Thus, in the present study, a "low strain rate" flame was defined as a flame for which the axial velocity gradient in the axial direction exhibits large regions where its value is about 10 s^{-1}. This choice of strain rate is consistent with the work of Chelliah et al., who used the axial velocity gradient on the oxidizer side of a pure counterflow diffusion flame to characterize the strain rate [39]. The strain rates were maintained near 10 s^{-1} based on the order of magnitude of the strain rate in large regions of coflow jet flames [32].

The method used in the present study to achieve low strain rates consisted of imposing a gradient in the radial velocity with respect to the radial distance at the nozzle entrances. This involved changing an Oppdif boundary condition, the proportionality constant between the radial velocity and the radius assumed as part of the similarity solution. Mathematically, this amounts to setting the value of (v/r) or $(-G/\rho)$ at each boundary to a nonzero value (see Eqs. 9 and 10). Physically, this amounts to imposing an outward radial velocity component at each nozzle, at locations away from the centerline, which increases with increasing distance away from the centerline (See Fig. 1). This is a variation from the usual plug flow boundary. The Oppdif boundary condition was changed using trial and error until a low strain rate condition was found. To the authors' knowledge, the present study represents the first investigation of flames employing an externally imposed nonzero radial velocity gradient at the fuel and air nozzles for the Oppdif formulation.

The selected operating conditions yielded nozzle velocities of 5 cm/s with nozzle radial velocity gradients set to 12 s^{-1}. To achieve different levels of partial premixing, these fluid mechanic boundary conditions were kept constant while the proportions of fuel and air in the fuel nozzle were changed to obtain a range of rich equivalence ratios between $\Phi_B = 1.6$ and ∞. Once a solution was obtained for the $\Phi_B = 1.6$ flame, this solution was used as an initial guess for the next computation, which was performed for an incrementally larger value of equivalence ratio. The temperatures at the boundaries were maintained at 300 K, and the nozzle separation distance was fixed at 2 cm. Representative results from flames with $\Phi_B = 1.6$, 1.8, 2.0, and 3.5, and from the pure diffusion flame are detailed in this paper.

It is worth mentioning that one characteristic of counterflow burners is that a radial outflow of species exists. This results in unburned fuel (CH_4) bypassing the flame. The fuel bypass fraction, calculated according to the method recommended by Takeno and Nishioka using the terms in the denominator of Eq. 14, ranged from 23% of the fuel injected in the $\Phi_B = 1.6$ flame to greater than 90% for the pure diffusion flame. This is in agreement with the findings of Dupont et al. [29], who found that for partially premixed flames with strain rate of about 10 s^{-1} the bypass fraction ranged from about 40% for $\Phi_B = 1.56$ to about 90% for the pure diffusion flame. While this fuel bypass affects the total amount of fuel burned, it should not affect the key structural features of the flames discussed in this paper.

RESULTS AND DISCUSSION

Flame Structure

Figure 2 shows centerline velocity profiles computed for the $\Phi_B = 1.6$, 1.8, 2.0, 3.5, and pure diffusion flames. The symbols shown on the pure diffusion flame curve in Fig. 2 are included to provide visual contrast between curves in this and other figures throughout this paper. All five

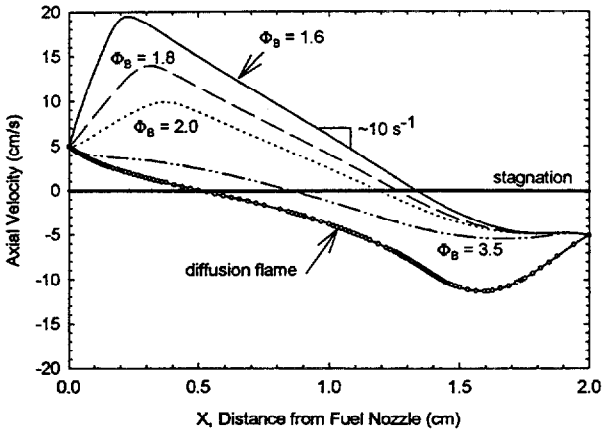

Fig. 2. Centerline axial velocity profiles for Φ_B = 1.6, 1.8, 2.0, and 3.5 flames, and for the pure diffusion flame.

of these velocity curves exhibit large central spatial regions where the centerline velocity gradient is between 5 s^{-1} and 15 s^{-1}. Thus, low strain rate partially premixed flames can be stabilized by imposing a radial velocity gradient at the fuel and air nozzles.

One interesting feature of Fig. 2 is that the "S-shaped" acceleration region that is usually prominent in counterflow flame velocity profiles [e.g., see Fig. 12 of Ref. 40, Fig. 2 of Ref. 41, and Figs. 2 and 3 of Ref. 42] is not apparent in any of these flames. This is surprising considering that the partially premixed flames of Tanoff et al. *did* exhibit profiles similar to the "S-shape" [31]. The top panel of Fig. 3 depicts the velocity profile for the Φ_B = 1.6 flame with and without the imposed radial velocity gradient at the nozzles. The figure shows that for the flame with no imposed gradient ($-G/\rho$ = 0 s^{-1}), the velocity profile is similar to those computed by Tanoff et al. Thus, the imposed radial velocity gradient at the fuel and air nozzles in the present flames causes the flat velocity profiles. It is instructive to further investigate the velocity gradients in this flame. The middle panel of Fig. 3 depicts the profile of the axial gradient of the axial velocity (du/dx), while the bottom panel of Fig. 3 shows the radial gradient of the radial velocity (dv/dr) for the Φ_B = 1.6 flame. For the flame with imposed radial gradients at the nozzles, both (du/dx) and (dv/dr) exhibit values of about 10 s^{-1} in large central spatial regions. It is apparent from the bottom panel of the figure that imposing nonzero radial velocity gradients at the fuel

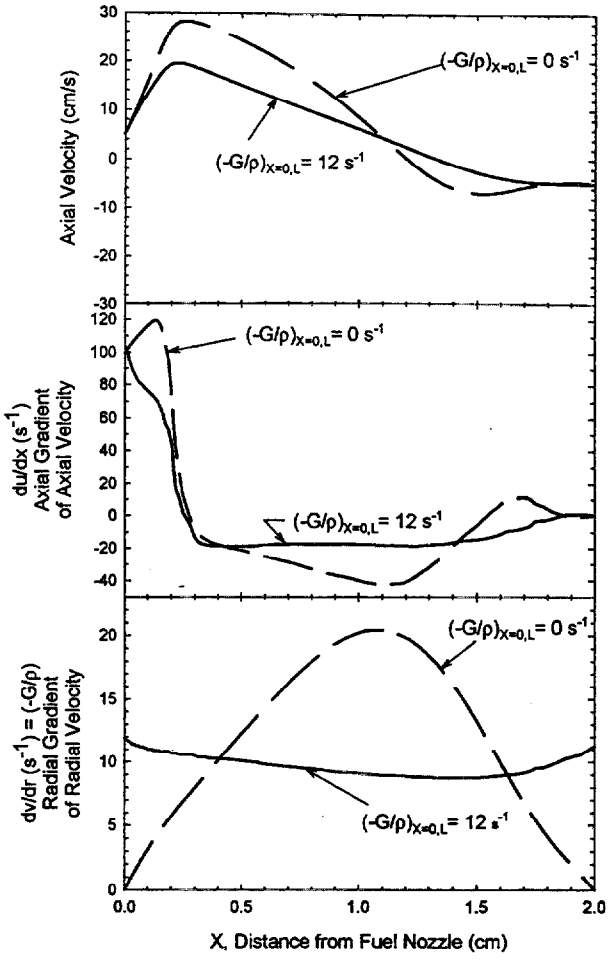

Fig. 3. Velocity profiles, axial velocity gradients, and radial velocity gradients for Φ_B = 1.6 flame with and without an imposed radial velocity gradient at the fuel and air nozzles.

and air nozzles causes the radial velocity gradient to remain essentially constant between the nozzles. This behavior leads to less steep gradients in the axial velocity and results in large regions of low strain rate in the flames.

Axial centerline temperature and major species mole fraction profiles are depicted in Fig. 4 for the Φ_B = 1.6 flame to show the general structure of the low strain rate partially premixed flames. The temperature rises on the fuel side with a steep slope to an inner characteristic temperature of about 1800 K, increases with a moderate slope of about 400 K/cm to a peak of 2090 K, and then smoothly reduces to 300 K at the air nozzle. The shape of this temperature profile is similar to those measured and computed in laminar double flames previously [3–5, 17, 28, 29, 31, 43]. The steep temperature gradients near the fuel and air nozzles are

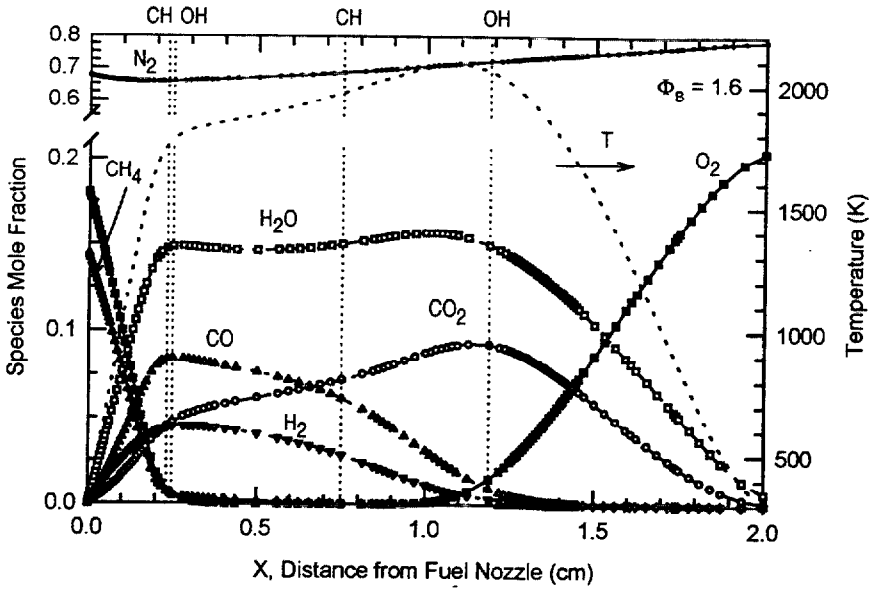

Fig. 4. Major species profiles and temperature for $\Phi_B = 1.6$ partially premixed CH_4/air flame. Dashed lines mark the locations of CH and OH radical concentration peaks.

indicative of heat transfer to the nozzles. As the fuel-side equivalence ratio is increased, the temperature profile becomes less steep near the fuel nozzle and more steep near the air nozzle. For the $\Phi_B = 1.6$ flame shown in the figure, the premixed CH_4/air flame exists near $x = 0.25$ cm and the CO/H_2/air nonpremixed flame exists near $x = 1.2$ cm. As Φ_B is increased in the present partially premixed flames toward a pure diffusion flame, the reaction zones blend together into narrower regions. In the pure diffusion flame, all species concentration peaks occur in or very near a single, narrow reaction zone.

Two interesting points can be made about the CO_2 and H_2O profiles shown in Fig. 4. First, the peak CO_2 and H_2O concentrations are about 10% and 15%, respectively. Since these two species have high concentrations in regions where temperature is high, gas band radiation losses could be significant in the present flames. If radiation heat transfer were considered in the present modeling, lower temperatures would result. Thus, it is important to consider that one of the limitations of the present Oppdif model is that radiation heat transfer is neglected. The second interesting point is that the CO_2 and H_2O concentrations do not become zero at $x = 2$ cm. This occurs because these two species diffuse into the air nozzle.

The vertical dashed lines in Fig. 4 represent locations of local CH and OH radical concentration peaks. Each of these intermediate species exhibits two peaks in its concentration profile for the $\Phi_B = 1.6$ flame. Tanoff et al. reported two peaks in the OH profile but only one peak in the CH profile for their computed counterflow flame with $\Phi_B = 2.0$ and ~150 s^{-1} strain rate [31]. Based on the conventional understanding that all hydrocarbons are consumed in the CH_4/air premixed flame zone of a double flame, indeed only one CH radical concentration peak at the CH_4/air premixed flame location is expected. The double CH radical peak behavior is a surprising characteristic of the present low strain rate flames, and has been reported in only one other study by Dupont et al. [29].

Figure 5 depicts CH radical concentration and temperature profiles for the $\Phi_B = 1.6$, 1.8, 2.0, 3.5, and pure diffusion flames. For the $\Phi_B = 1.6$ flame, the primary CH concentration peak of 0.07 ppm (parts per million or μL/L) exists at 0.25 cm, with a smaller secondary peak of 0.01 ppm emerging at 0.8 cm. For the $\Phi_B = 1.8$ flame, there are smaller (~0.02 ppm) but equal CH concentration peaks. For the $\Phi_B = 2.0$ flame, the peak of 0.03 ppm at about 0.9 cm is much larger than the peak near 0.5 cm. The $\Phi_B = 3.5$ and pure diffusion flames exhibit only one CH radical concentration peak near the fuel nozzle, with magnitudes of 0.10 ppm at 1.1 cm and 0.40 ppm at 1.45 cm, respectively.

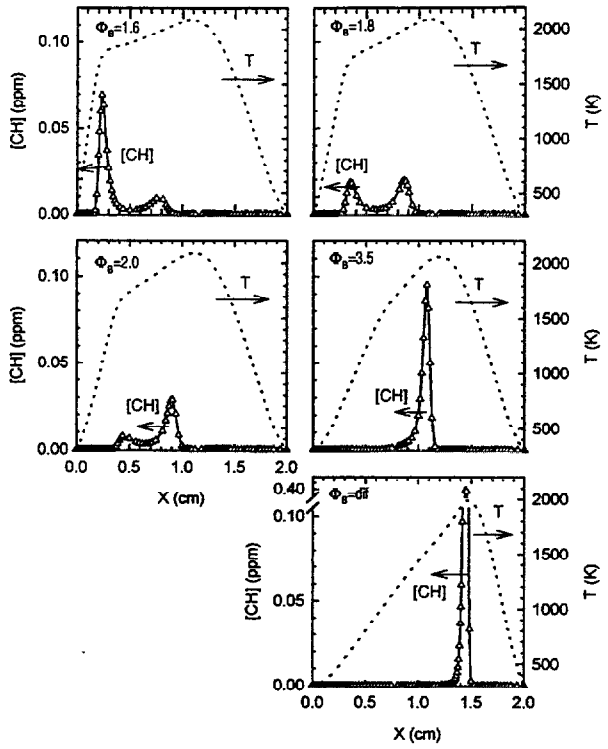

Fig. 5. CH concentration profiles and temperature profiles for Φ_B = 1.6, 1.8, 2.0, and 3.5 flames, and for the pure diffusion flame.

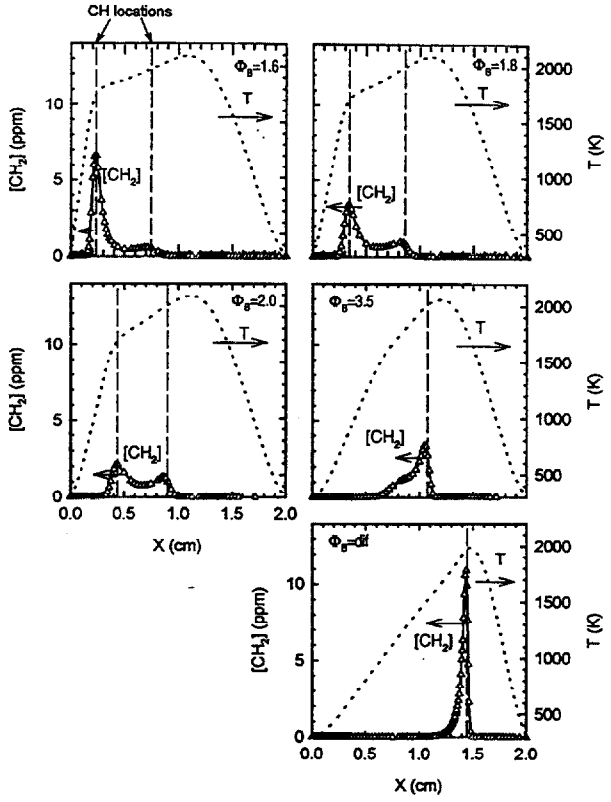

Fig. 6. CH_2 concentration and temperature profiles for Φ_B = 1.6, 1.8, 2.0, and 3.5 flames, and for the pure diffusion flame. Dashed lines mark CH concentration peak locations.

Thus, for intermediate levels of partial premixing, double CH radical peaks with very low concentrations occur. At this point, it is worth noting that the reaction rates in GRI-Mech 2.11 were optimized by Bowman et al. to predict the peak CH radical concentration, the location of this peak CH concentration, and the halfwidth of the CH profile in low pressure, laminar, premixed $CH_4/O_2/N_2$ flames [22]. In the present flames, as the fuel side equivalence ratio is increased, the CH radical concentration peak nearest the fuel nozzle decreases in magnitude while the CH peak near the air nozzle increases in magnitude. Both CH peaks move away from the fuel nozzle as the fuel-side equivalence ratio increases. The double radical peaks are caused by CH_4, CH_3, and CH_2 (CH_i) surviving the premixed flame zone and reacting in between the two traditionally defined combustion zones of the "double flame." Close examination of Fig. 4 reveals that a small but finite concentration of CH_4 survives the premixed reaction zone and enters the region between the double flames. Figures 6 and 7 depict the CH_2 and CH_3 profiles for the present flames, respectively. Temperatures and CH peak locations are shown. The figures demonstrate that CH_2 exhibits double peak behavior, while CH_3 exists throughout the zone between the CH peaks.

To gain a better understanding of this flame structure, CH_4 molar production rates are graphed in Fig. 8. Negative values of the production rate indicate consumption. Temperature profiles are shown for reference, and vertical dashed lines mark the locations of CH concentration peaks. For the Φ_B = 1.6 flame, the CH_4 is mostly consumed in the premixed flame. There is also a consumption of CH_4 at the location of the second CH peak which is difficult to discern in the figure because of the large scale of the ordinate axis. The Φ_B = 1.8 and 2.0 flames exhibit similar CH_4 consumption behavior, but the rate of CH_4 consumption in the central region increases with increasing Φ_B. The Φ_B = 3.5 CH_4 consumption curve exhibits two prominent CH_4 consumption peaks. As already seen, the larger (compared to CH)

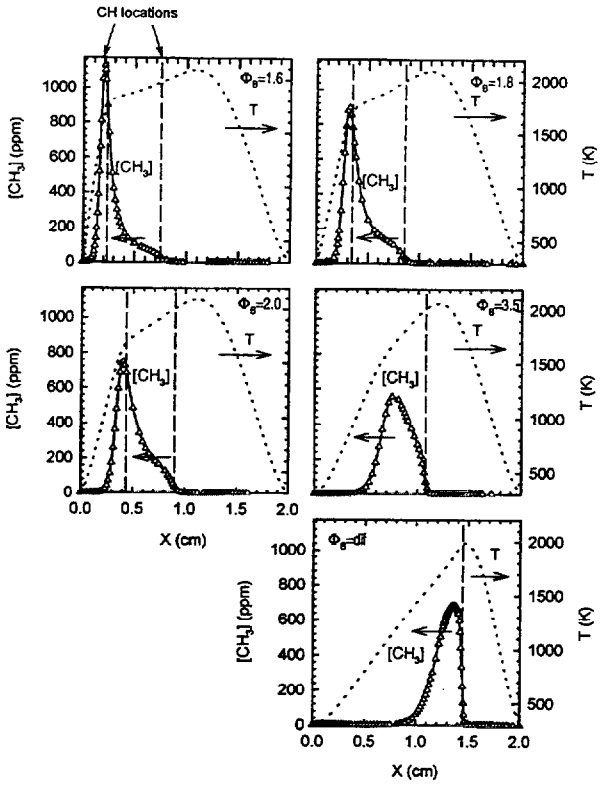

Fig. 7. CH_3 concentration and temperature profiles for Φ_B = 1.6, 1.8, 2.0, and 3.5 flames, and for the pure diffusion flame. Dashed lines mark CH concentration peak locations.

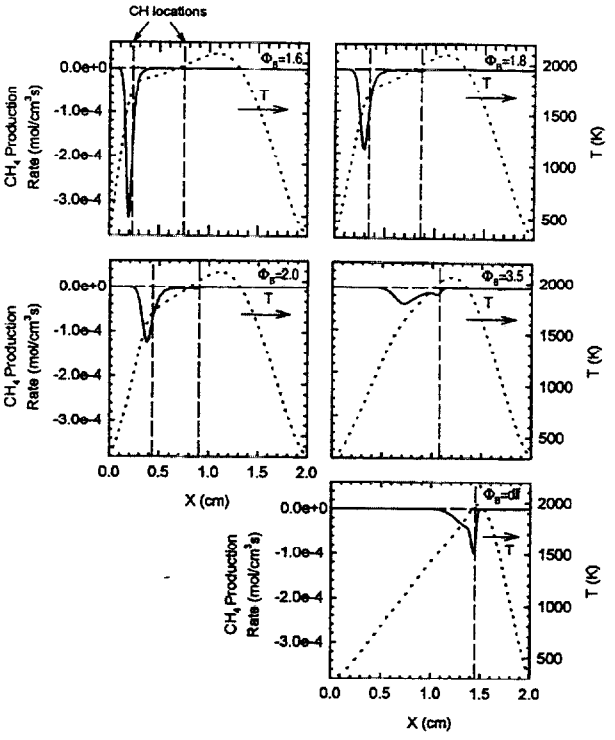

Fig. 8. CH_4 production rate and temperature profiles for Φ_B = 1.6, 1.8, 2.0, and 3.5 flames, and for the pure diffusion flame. Dashed lines mark CH concentration peak locations.

hydrocarbon fragments such as CH_3 and CH_2 exist at the point of CH_4 consumption near 0.7 cm for the Φ_B = 3.5 flame, even though there is no CH concentration peak here. The CH_4 consumption region for the pure diffusion flame spans a width of about 0.5 cm.

Figure 9 depicts CO production rates for the five flames of interest. In the Φ_B = 1.6, 1.8, and 2.0 flames (the ones with double CH peaks), there is a zone of CO formation near each CH peak. The CO is consumed near the temperature peak. The Φ_B = 3.5 flame exhibits one CO formation zone on the fuel side of the single CH peak, one CO formation zone at the location of the single CH peak, and one CO destruction zone near the temperature peak. The pure diffusion flame (Φ_B = ∞) forms CO at the location of the CH peak and consumes CO on the air side of the CH peak. While not shown here, H_2 production rate profiles exhibit similar behavior. These profiles demonstrate that in a partially premixed flame, CO and H_2 are formed in the CH_4/air premixed flame and consumed in the CO/H_2/air nonpremixed flame, which is in agreement with conventional understanding of double flames.

Further insight into the flame structure can be gained from the O_2 production rate profiles shown in Fig. 10. Temperature profiles are shown, and the vertical dashed lines indicate CH peak locations. For all flames except the pure diffusion flame, two distinct oxygen consumption zones exist. Based on inspection of Fig. 10, one of these two zones is associated with the CH_4/air premixed flame and the other with the CO/H_2/air nonpremixed flame. For the three flames that exhibit double CH concentration peaks (Φ_B = 1.6, 1.8, and 2.0), the central CH peak occurs at the inside edge of the O_2 consumption zone associated with the CO/H_2/air nonpremixed flame. The single peak of the Φ_B = 3.5 flame also exists at the inside edge of this zone. Figure 11 depicts mole fraction profiles of key flame radicals, H atom, OH radical, and O atom (×4), for the Φ_B = 1.6 flame. Temperature and CH peak locations are included. The two flame zones corresponding to

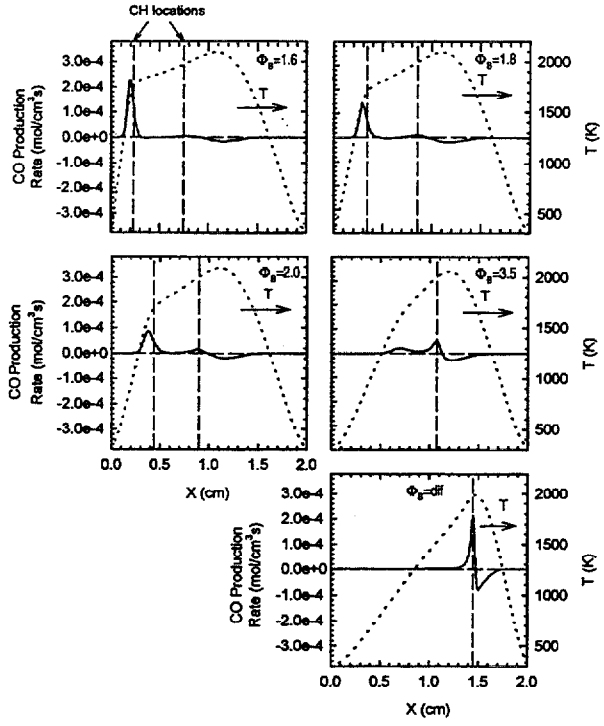

Fig. 9. CO production rate and temperature profiles for Φ_B = 1.6, 1.8, 2.0, and 3.5 flames, and for the pure diffusion flame. Dashed lines mark CH concentration peak locations.

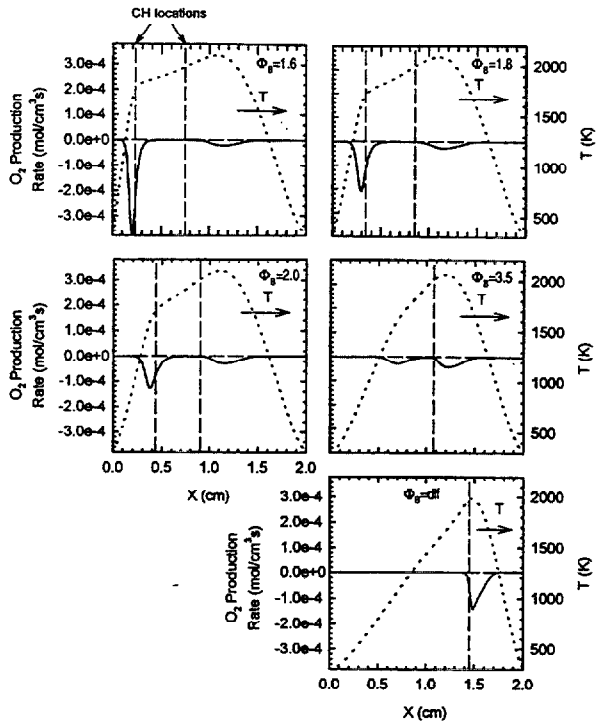

Fig. 10. O_2 production rate and temperature profiles for Φ_B = 1.6, 1.8, 2.0, and 3.5 flames, and for the pure diffusion flame. Dashed lines mark CH concentration peak locations.

the two distinct O_2 consumption zones are evident from the double peaked H, OH, and O profiles in the figure. Each CH radical peak is associated with one of these flame zones. Although not shown in this paper, enlarging the scale of the molecular O_2 profiles in the vicinity of the central CH peak revealed that the O_2 reacting with CH_4 at this location originates in the air nozzle and penetrates across the stagnation point and into the rich region of the CO/H_2/air nonpremixed flame. The O_2 penetration into the counterflow flame is in agreement with previous results from pure diffusion flames [40]. Thus, it can be inferred that the CH peak nearest the fuel nozzle "belongs" to the CH_4/air premixed flame, while the CH peak nearest the air nozzle "belongs" to the CO/H_2/air nonpremixed flame. This is a unique computed structure which to the authors' knowledge has not been detailed previously. Hereafter in this paper, the CH peak near the CH_4/air premixed flame location will be referred to as the "premixed flame CH peak," and the CH peak near the edge of the CO/H_2/air nonpremixed flame oxidation zone will be referred to as the "nonpremixed flame CH peak."

Figure 12 depicts a summary of the location of the stagnation plane, the location of the temperature peak, the locations of the CH and OH radical peaks, and the region for which the premixed CH_4 and air mixture is flammable (at room temperature and atmospheric pressure) with Φ_B = 1.6–4.0. The flammable region is defined as the region in which the methane fuel to air ratio on a mass basis is between 0.0268 and 0.0955 [44]. The following equation defines the fuel to air ratio, with X_j and MW_j representing the mole fraction and molecular weight of species j, respectively:

$$FA = \frac{X_{CH_4} MW_{CH_4}}{X_{O_2} MW_{O_2} + X_{N_2} MW_{N_2}} \tag{15}$$

Two interesting points about the structure of low strain rate partially premixed flames are inferred from Fig. 12. First, the premixed flame CH peak occurs outside of the region where the CH_4/air mixture is flammable at room temperature. Although not shown on the graph, the

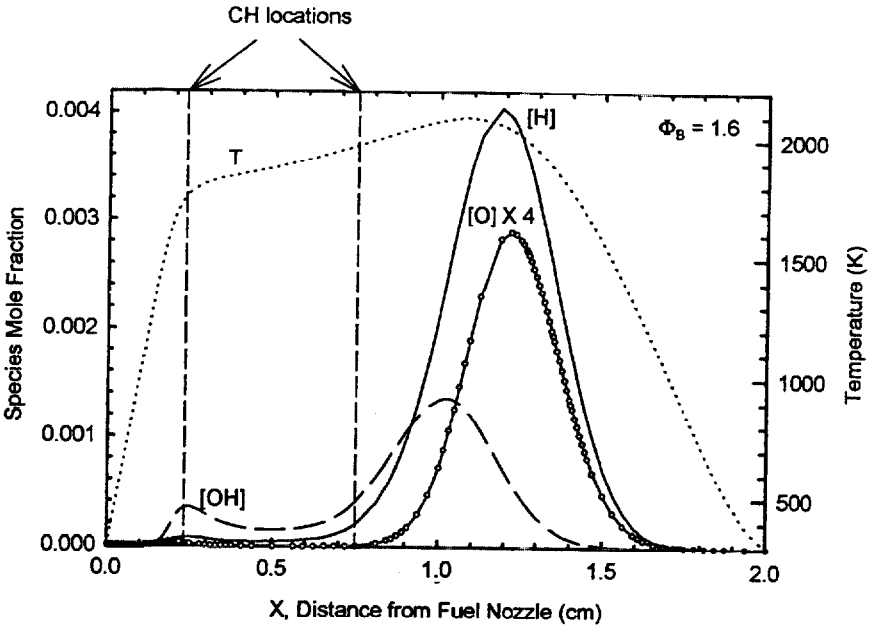

Fig. 11. Concentration profiles for H, O (×4), and OH radicals along with a temperature profile for $\Phi_B = 1.6$ partially premixed flame. Dashed lines mark CH concentration peak locations.

other CH_i radicals (i = 0, 1, 2, and 3) exhibit concentration peaks very near the CH peak and also outside of the flammable region for CH_4 and air. To the extent that hydrocarbon intermediates mark the reaction zone in a premixed flame, this behavior indicates that CH_4 combustion occurs outside of the traditionally defined flammability limits in these partially premixed flames, in agreement with results of previous studies [3, 31]. The second interesting feature of Fig. 12 is the relative positions of the stagnation plane and the flame zones. Beginning with $\Phi_B = 1.6$, as the premixed gas stream becomes more fuel-rich (Φ_B increases), the stagnation plane moves toward the fuel nozzle. In order to understand this behavior, it is useful to recall that there are two acceleration regions in a partially premixed flame: one associated with the heat release of the CH_4/air premixed flame near the fuel nozzle and the other associated with the heat release of the CO/H_2/air nonpremixed flame near the air nozzle. The location of the stagnation plane is strongly affected by the acceleration and peak

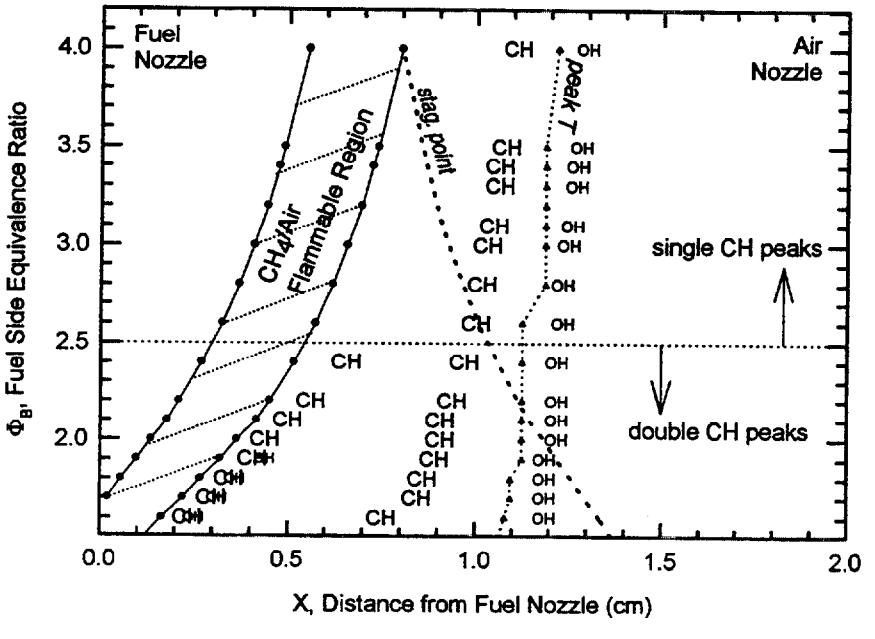

Fig. 12. Location of stagnation plane, temperature peak, CH and OH radical concentration peaks, and CH_4/air flammability region for low strain rate partially premixed flames. A horizontal dotted line marks the fuel-side equivalence ratio at the transition from single CH peak behavior to double CH peak behavior.

velocity achieved in the CH_4/air premixed flame. As the premixed gas stream becomes more fuel-rich, the acceleration and the maximum velocity experienced by the premixed flame lessen. As these become smaller, deceleration of the fuel-side gases to zero velocity requires a smaller physical distance. Hence, the stagnation point moves toward the fuel nozzle. This explanation is supported by the findings of Tanoff for partially premixed flames with higher strain rates [31]; these authors reported that the structure of their flames was dominated by the fuel-side velocity gradient of the premixed flame. The double CH radical peaks always occur together on the fuel side of the stagnation plane. For flames with Φ_B greater than 2.5, CH radical is no longer formed by the CH_4/air premixed flame, and only the nonpremixed flame CH radical peak exists. The CH_4/air premixed and CO/H_2/air nonpremixed flames begin to merge, although the O_2 consumption profiles demonstrate that there are still two distinguishable flame zones. The flames with Φ_B greater than 2.5 are termed "merged" flames in the present paper, although it is important to note that two flame zones are still distinguishable. The merged flame crosses over onto the oxidizer side of the stagnation plane, which is the expected position relative to the stagnation plane for a pure diffusion flame [40].

It is interesting to further compare the present flame structure with that discussed by Tanoff et al. [31]. These authors computed the sensitivity of flame structure to overall strain rate and equivalence ratio for $\Phi_B = 1.3$–2.0 and pure diffusion flames with strain rates between 100 and 900 s^{-1}. Their strain rate was defined based on the air side velocity gradient. These authors found that the structure was sensitive to the maximum *fuel*-side velocity gradient, and that this gradient could be used to predict the equivalence ratio corresponding to the transition from a double flame to a merged flame. At their lowest strain rate ($\sim 100\ s^{-1}$), the fuel-side velocity gradient ranged from about 200 s^{-1} for $\Phi_B = 2.0$ to about 3000 s^{-1} for $\Phi_B = 1.3$. They found that this configuration yielded a double flame below $\Phi_B = 1.5$, while it yielded a merged flame above this equivalence ratio. This "transition" fuel-side equivalence ratio increased with decreasing strain rate. In the present study, the maximum fuel-side velocity gradient ranged from 2 s^{-1} for $\Phi_B = 3.5$ to about 100 s^{-1} for $\Phi_B = 1.6$, and the transition from double flame to merged flame behavior occurred at $\Phi_B = 2.5$. The higher "transition" equivalence ratio for flames with the present low strain rate is consistent with the inverse dependence of this quantity on strain rate found by the above authors.

For pure diffusion flames, it is useful to express variables in terms of the mixture fraction (Z) and the scalar dissipation rate (SDR) [45, 46]. The present low strain rate partially premixed flames possess a hybrid structure between that of pure diffusion and that of pure premixed flames. Thus, it is of interest to present the mixture fraction and scalar dissipation behavior of the present flames for comparison to previous work on pure diffusion flames (see comments by Bilger and by Chen, Ref. 31). The mixture fraction is defined as the mass fraction that originated as CH_4 in the fuel stream, and is calculated as

$$Z = \sum_i Y_i(N_C)\left(\frac{\mathrm{MW}_C}{\mathrm{MW}_i}\right) + \sum_i Y_i(N_H)\left(\frac{\mathrm{MW}_H}{\mathrm{MW}_i}\right). \tag{16}$$

Here, N_C and N_H are the number of carbon and hydrogen atoms per mole of species i, respectively. This definition of mixture fraction yields a value of $Z = 0.055$ for stoichiometric conditions for CH_4. The scalar dissipation rate may be interpreted as the inverse of a characteristic diffusion time [47], and is defined for the present geometry as

$$\mathrm{SDR} = 2D\left(\frac{\partial Z}{\partial x}\right)^2 \mathrm{s}^{-1}. \tag{17}$$

Here, D is the species diffusion coefficient selected by Norton et al. [46] and by Bilger [45],

$$D \cong 1.786 \times 10^{-5} T^{1.662}\ \mathrm{cm}^2/\mathrm{s}. \tag{18}$$

This diffusion coefficient is a power-law fit to data for CO in O_2 [45]. For the purpose of finding the SDR, the spatial derivative of the mixture fraction is calculated using a simple truncated first-order Taylor series. This results in scattered values in areas of coarse grid reso-

lution or unevenly spaced grid points. No attempt was made to smooth the curves; the SDR behavior was explored here for the purpose of providing a general flame structure for comparison. Figure 13 depicts the mixture fraction and scalar dissipation rate profiles for the Φ_B = 1.6, 1.8, 2.0, 3.5, and pure diffusion flames. Temperature profiles are shown, and vertical dashed lines indicate the locations of the CH peaks. The range of the ordinate axis of the pure diffusion flame graph is larger than that used for the partially premixed flame graphs. For Φ_B = 1.6, SDR exhibits one peak at about 0.06 s^{-1} near the CO/H_2/air nonpremixed flame. For Φ_B = 1.8 and 2.0, a second peak appears in the SDR curve. For Φ_B = 3.5 a strong double peak structure is evident in the scalar dissipation rate, with both peaks having values less than 0.10 s^{-1}. This double peak structure is in qualitative agreement with scalar dissipation rate profiles calculated by Drake and Blint for $CO/H_2/N_2$/air counterflow pure diffusion flames with strain rates on the order of 10 s^{-1}, although the present peak SDR of 0.06 s^{-1} to 2.5 s^{-1} is lower than the 4 s^{-1} computed for their flames [42]. Figure 13 shows that the scalar dissipation rate peaks at 2.5 s^{-1} at an axial location of about 0.4 cm in the low strain rate pure diffusion flame. Norton et al. reported peak SDR values as high as 8 s^{-1} based on measurements performed in Wolfhard-Parker diffusion flames [46].

In summary, above Φ_B = 2.5, the present flame structure can be described as a CH_4/air premixed flame merged with a CO/H_2/air nonpremixed flame. Below Φ_B = 2.5, the two flame zones are more physically separate, and the CO/H_2/air nonpremixed flame contains a small region containing hydrocarbon concentration peaks on its fuel-side edge. While there are seemingly three characteristic combustion zones in this flame, it is not a "triple flame," in the classic sense. This is because the flow velocity is in a direction parallel to the mixture fraction gradient. In contrast, the velocity of a triple flame is perpendicular to the mixture fraction gradient. It also is not a "double flame," in the classic sense, because for some operating conditions there are two hydrocarbon concentration peaks. The present structure is best described as a special case of the partially premixed double flame. Nishioka et al. [48] stated that the general type of flame (in their case premixed, diffusion, and partially premixed) is the most important parameter for determining NO behavior. The next section of this paper describes how the unique structure reported in this paper might affect NO formation.

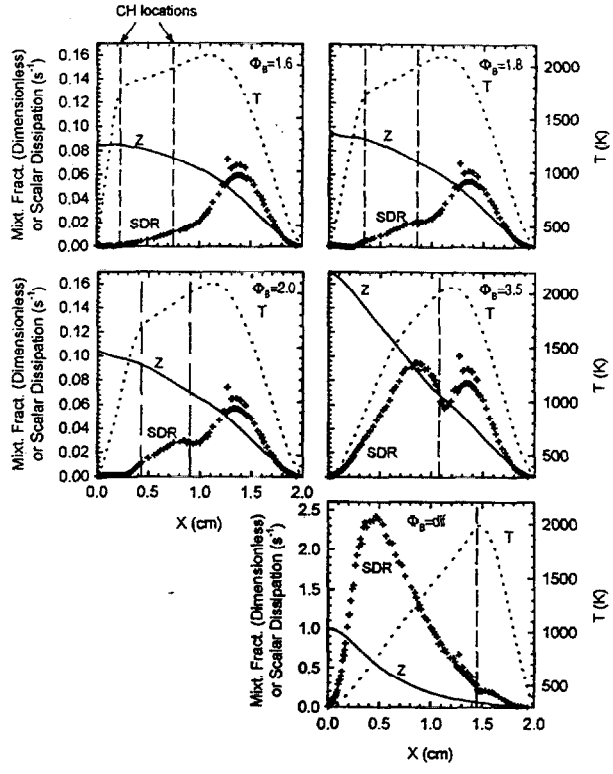

Fig. 13. Mixture fraction (Z) and estimated scalar dissipation rate (SDR) along with temperature profiles for Φ_B = 1.6, 1.8, 2.0, and 3.5 flames, and for the pure diffusion flame. Dashed lines mark CH concentration peak locations.

NO Formation

Figure 14 depicts the net NO production rate profiles for the Φ_B = 1.6, 1.8, 2.0, 3.5, and pure diffusion flames. Temperatures are shown, and the locations of the CH radical concentration peaks are marked. The range of the ordinate axis of the pure diffusion flame graph is larger than that for the other flames. The Φ_B = 1.6, 1.8, and 2.0 flames exhibit three significant NO reaction zones apiece. These are: (1) NO destruction beginning at the premixed flame location and persisting in the region between the double CH concentration peaks, (2) NO formation on the air side of the nonpremixed flame CH peak, and (3) NO formation

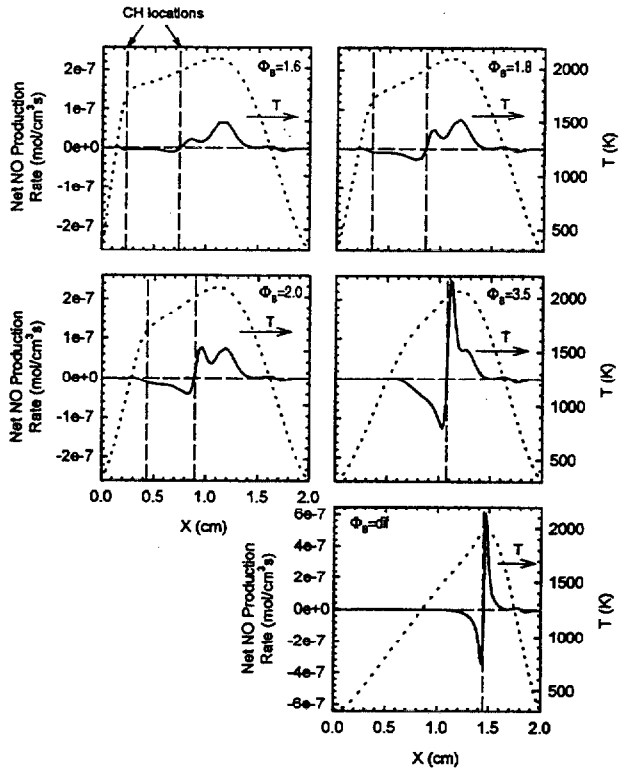

Fig. 14. Net NO production rate and temperature profiles for Φ_B = 1.6, 1.8, 2.0, and 3.5 flames, and for the pure diffusion flame. Dashed lines mark CH concentration peak locations.

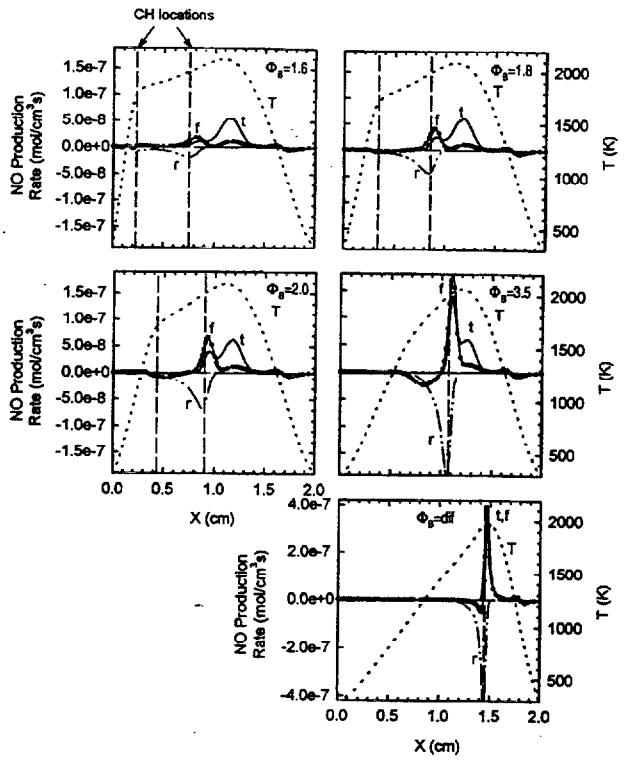

Fig. 15. Local NO production rates via three thermal reactions (t), 13 reburn reactions of the type CH_i + NO (r), and 22 remaining reactions which include but are not limited to Fenimore reactions (f), along with temperature profiles for Φ_B = 1.6, 1.8, 2.0, and 3.5 flames, and for the pure diffusion flame. All curves computed using full N_2 chemistry. Dashed lines mark CH concentration peak locations.

near the nonpremixed flame temperature peak. The Φ_B = 3.5 flame exhibits a wide NO destruction zone on the fuel side of the CH peak and two overlapping but individually distinguishable NO formation zones on the air side. The pure diffusion flame contains a single narrow NO destruction zone on the fuel side and a single narrow NO formation zone on the air side of the CH concentration peak, similar to that measured in a Wolfhard-Parker coflow burner [21] and predicted for counterflow flames [28]. For each operating condition shown in Fig. 14, the dividing point between the region of NO destruction and the region(s) of NO formation occurs at the location of its nonpremixed flame CH peak. The small formation and destruction zones near the air nozzle for all flames at temperatures near 1200 K result from the interconversion of NO with NO_2; the existence of these zones is in qualitative agreement with the calculations performed at higher strain rates by Nishioka et al. [28].

A more detailed analysis reveals that the NO destruction zones are caused primarily by reactions of NO with hydrocarbon fuel fragments denoted by CH_i(i = 0, 1, 2, and 3). These reactions are commonly called "reburn" reactions [21, 30]. Figure 15 shows the results of the more detailed analysis. Temperature profiles are shown, CH peak locations are indicated, and the range of the ordinate axis is larger for the pure diffusion flame than for the other flames. In the figure, the curve marked t represents the contribution of the thermal NO mechanism, and is the net sum of the reaction rates, during the full calculation, from GRI-Mech 2.11 reactions numbered 178 to 180. The curve marked r represents the reburn reactions, and is the sum of the reaction rates of the 13 CH_i + NO reactions (GRI-Mech 2.11 numbers 244 to 256). The curve marked f is the sum of the kinetic rates of the 22 additional reactions involving NO that are included in GRI-Mech 2.11. These reactions include but are not limited to the Fenimore mechanism, the N_2O mechanism (GRI-Mech reaction numbers 182, 199,

and 228), and the reactions that involve the interchange between NO and NO_2 (GRI-Mech reaction numbers 186 to 189). Strictly isolating the contribution of the Fenimore reactions (sometimes called "prompt") to NO formation is difficult because Fenimore initiation reactions form intermediate species (N, HCN, etc.) which can participate in the thermal and in other reaction pathways. Since the NO mechanisms share common species and thus affect each other, no attempt is made in the present work to assign percentages to the relative contributions of each one to the total amount of NO formed. The far more interesting result here is the spatial distribution of the NO reaction rates and the regions where the different NO mechanisms come to bear.

Several interesting points can be made about Fig. 15. First, as previously stated, the NO destruction zones are caused by CH_i + NO reburn reactions. The reburn species leading to the most rapid NO consumption is CH_2, in agreement with the findings of Dupont et al. [29]. The reburn zones are significant because of their physical location; NO is produced in the formation zone(s) and is transported into the physically separate destruction zone before it is consumed. The second interesting feature of Fig. 15 is that the NO formation zone near the nonpremixed flame CH peak in the partially premixed flames is contributed to by both the thermal mechanism and by the reaction set which includes the Fenimore mechanism. The temperatures at the reaction rate peak in this zone are 2000 K in the Φ_B = 1.6 flame, 2024 K in the Φ_B = 1.8 flame, 2028 K in the Φ_B = 2.0 flame, 2035 K in the Φ_B = 3.5 flame, and 1986 K in the pure diffusion flame. All of these temperatures are above the 1800 K minimum usually estimated as the limit for thermal NO formation. Thus, the fact that the temperature is above the threshold for thermal NO formation does not mean that NO formation is dominated by the thermal mechanism. The final point worth noting is that there are NO destruction features in the Φ_B = 2.0, 3.5, and pure diffusion flames which are caused by the reactions that include the Fenimore mechanism. A thorough analysis revealed that these negative NO reaction rates result almost entirely from

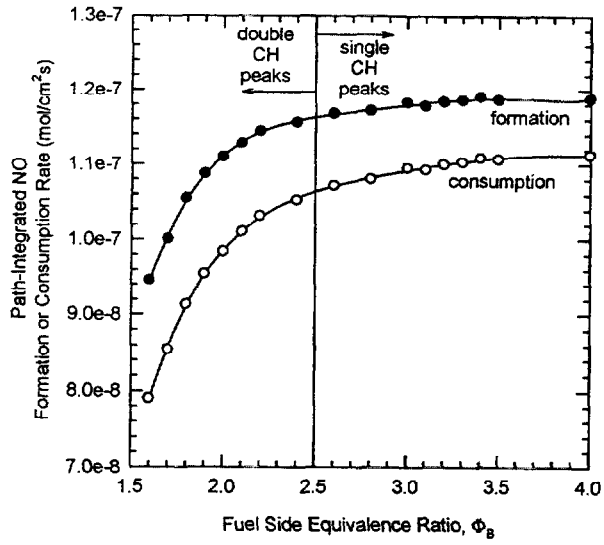

Fig. 16. Path-integrated NO formation and consumption rates for low strain rate partially premixed flames with Φ_B = 1.6–4.0. A vertical line marks the transition from double CH peak behavior to single CH peak behavior.

consumption of NO by reaction number 274 in GRI-Mech 2.11:

$$HCCO + NO \Leftrightarrow HCNO + CO \qquad (19)$$

This reaction was termed the "initiation reaction of the HCN recycle route" for NO by Nishioka et al. [48].

The present flame structure is intriguing because it implies that the reburn NO consumption zone can be narrowed or broadened through control of the fluid mechanic strain rate and the amount of air mixed in with the fuel. From a practical standpoint, if one could physically increase the separation distance between the NO formation and destruction zones and broaden the destruction zone to increase its influence, NO could be formed in one portion of a flame and then transported into the destruction zone as a way to abate Fenimore NO. This proves to be an overly optimistic goal, however, because moving and broadening the CH_i + NO destruction zone does not necessarily increase its influence on the net amount of NO formed in the flame. This point is demonstrated in Fig. 16, which depicts the integrated net NO formation and consumption rates for the present flames. Regardless of the number of CH radical peaks or the location or width of the NO destruction zone, the net formation rate is higher than the net consumption rate for every

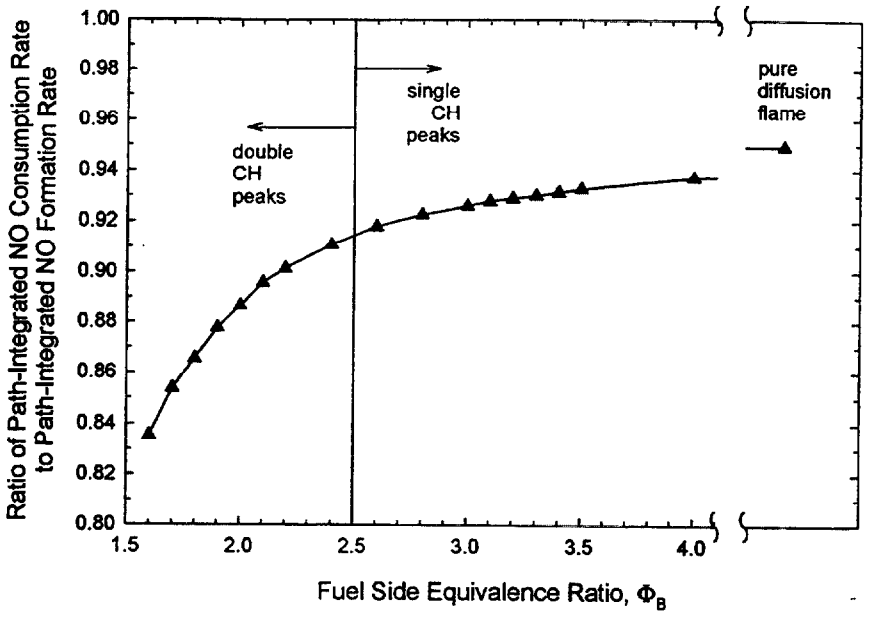

Fig. 17. Ratio of the path-integrated NO consumption rate to the path-integrated NO formation rate as a function of fuel-side equivalence ratio.

partially premixed flame. Figure 17 shows the ratio of the net integrated NO consumption rate to the net integrated NO formation rate as a function of fuel-side equivalence ratio. There is no obvious change in the curve of Fig. 17 at $\Phi_B = 2.5$, so the flame structure change does not strongly affect the relative importance of the NO destruction reactions. The figure demonstrates that the importance of NO destruction relative to NO formation increases with increasing fuel-side equivalence ratio. In fact, NO destruction is more important for the pure diffusion flame than for the partially premixed flames.

The use of the term "reburn" to describe CH_i + NO reactions is borrowed from the practical NO abatement technology known as "reburn" or "fuel-staging" used to achieve 50–70% NO reduction in full-scale furnaces and boilers [49–51]. In this strategy, the fuel and air burn in a slightly fuel-lean *primary zone*, followed by a rich *reburn zone* where extra fuel (typically natural gas) is injected, and then enter a *burnout zone* where additional air is injected. In the *burnout zone*, most of the NO, HCN, and NH_3 are converted to N_2 in a low-temperature reaction. The temperature in the *burnout zone* must be kept at or slightly below 1200 K in order to effectively convert the fixed nitrogen species to molecular N_2 [50]. In contrast, in a flame, the low-temperature *burnout zone* may not exist. The fixed nitrogen species (e.g., HCN) in the present laminar flames are transported into a high-temperature region where they are likely to recycle into NO. Thus, an NO abatement strategy would not only involve physically separating the consumption and formation zones in the flame; it would also involve forcing the intermediates formed by the consumption reactions to progress toward N_2 rather than the preferred NO at high temperatures. Inducing the latter behavior becomes the challenge.

Because of the fact that the CH_i + NO reactions form intermediate chemical species that are likely to form NO again, some researchers have chosen to define the "reburn" reactions as ones that consume NO and directly terminate into molecular N_2 such as NH_i + NO (i = 0, 1, and 2) [52].

Figure 18 shows the net NO_x formation rate, the net CH_4 consumption rate, and the calculated $EINO_x$, which is the ratio of the first two terms, as a function of fuel-side equivalence ratio. The curves of Fig. 18 experience a change in slope at the point where the CH radicals switch from double to single peaks. The change in slope of the CH_4 consumption rate curve at $\Phi_B = 2.5$ indicates a change in the flame structure, while the change in slope of the net NO_x formation rate curve indicates a corresponding change in the NO_x formation behavior. However, as previously shown in this paper,

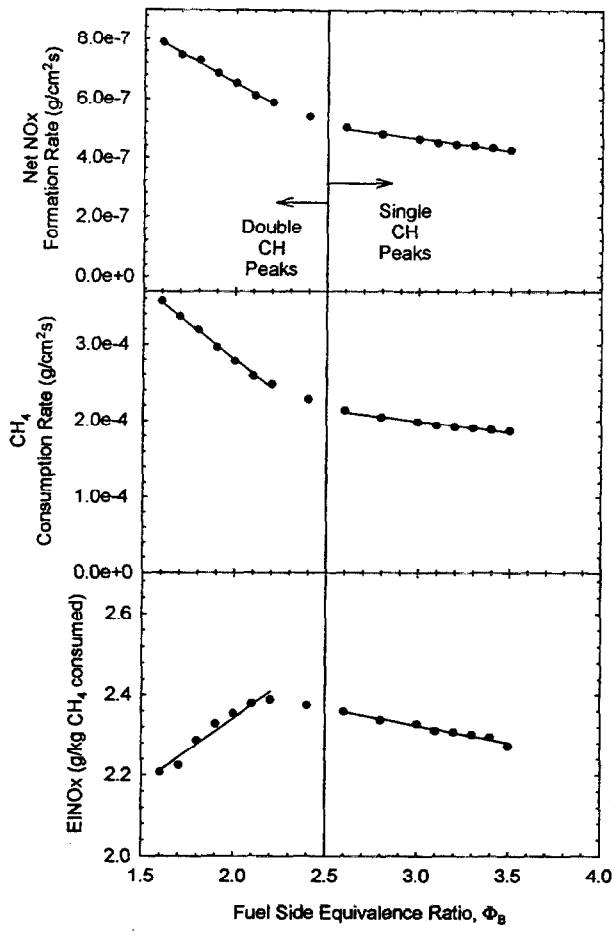

Fig. 18. Net NO_x ($NO + NO_2$) formation rate, net CH_4 consumption rate, and NO_x emission index for low strain rate partially premixed flames with Φ_B = 1.6–3.5. Vertical lines mark the transition from double CH peak behavior to single CH peak behavior.

the change in the NO_x behavior is not necessarily caused by NO destruction reactions.

The $EINO_x$ results range between 2.2 g/kg and 2.5 g/kg of fuel, and are higher than the values measured for coflow partially premixed flames (0.8 g/kg to 2.0 g/kg fuel) [14, 15] and those computed for counterflow partially premixed flames (0.5 g/kg to 1.0 g/kg fuel) [28]. The higher $EINO_x$ for the present lower strain rate flames is consistent with previous findings that total $EINO_x$ becomes larger as strain rate is lowered [28]. Although not shown in the figure, the $EINO_x$ for the pure diffusion flame is about 1.6 g/kg of CH_4 burned, which is consistent with the importance of destruction reactions in this flame reported earlier in this paper. Figure 18 shows that the present flames exhibit a local $EINO_x$ *maximum* at Φ_B = 2.5, in contrast to the exhaust $EINO_x$ minimum measured at about Φ_B = 2.0 in laminar and turbulent coflow partially premixed flames [14–16]. These two results do not necessarily contradict each other since the present emission indices are spatially integrated quantities for counterflow flames with low strain rates, while the experimental emission indices are global exhaust measurements for coflow flames which exhibit a range of low to high strain rates. The $EINO_x$ computations for counterflow flames depend strongly on the fuel bypass behavior, while the assumption is made that all fuel is completely burned in a coflow flame. This comparison draws attention to the difficulty of interpreting $EINO_x$ data from counterflow flames where bypass flows of fuel (CH_4) and intermediates (CO, H_2, etc.) escape before combustion is complete. For this reason, emission index results from the two types of flames must be compared cautiously.

COMPARISON WITH PAST STUDIES AND FURTHER DISCUSSION

The double CH radical peaks of the present study agree qualitatively with those in large-domain, low strain rate flames reported by Dupont et al. [29]. These authors found double CH peaks when the strain rate, calculated as the eigenvalue of the problem [26], was varied between 10 s^{-1} and 20 s^{-1}. They found the double peaks using the GRI-Mech 2.11 mechanism and using the Miller-Bowman mechanism [30]. Thus, the unique low strain rate partially premixed flame structure has been computed (1) in flames with different physical mechanisms used to create low strain, and (2) with different chemical mechanisms.

It is useful to compare the results of the present study with those from Nishioka et al. [28]. Their higher strain rate flames (u = 16 cm/s, Φ_B = 1.5 to infinity) exhibited (1) an NO destruction zone on the reactant side of the CH_4/air premixed flame, (2) an NO formation zone on the air side of the CH_4/air premixed flame, and (3) an NO formation zone near the CO/H_2/air nonpremixed flame temperature peak. Their lowest strain rate flame (5 cm/s nozzle exit velocity, Φ_B = 1.80) exhibited these same

zones, except that zone (1) was physically broadened relative to the high strain rate cases. The present partially premixed flames exhibit the same basic NO reaction zones, except the locations of the zones change when there are two CH peaks. The flames with double CH peaks exhibit (1) an NO destruction zone which *begins* on the reactant side of the CH_4/air premixed flame and persists throughout the broad region *between* the two CH peaks, (2) an NO formation zone on the air side of the CO/H_2/air nonpremixed flame CH peak, and (3) an NO formation zone near the CO/H_2/air nonpremixed flame temperature peak. Thus, the results of the present study agree qualitatively with the broadening of the NO destruction zone at lower strain rates found by Nishioka et al.

To the authors' knowledge, this intriguing calculated flame structure has not been identified experimentally in any laboratory flames. It would be interesting if the existence of double CH peaks could be confirmed experimentally. Modern methods such as LIF can be used to effectively locate double CH radical peaks if they indeed exist in laboratory flames. It is recognized that stabilizing low strain rate counterflow flames by imposing radial velocity gradients at the nozzles presents an experimental challenge. Chelliah et al. stated that radial velocity components were present at the fuel nozzle for pure diffusion flames established on small burners, while flames established on large burners resulted in plug flow [39]. Thus, varying the size of the counterflow burner may be a way to obtain radial velocity gradients at the fuel and air nozzles and thus achieve low strain rates. Increasing the nozzle separation distance is another way to establish low strain rate counterflow flames. It should be noted that the present analysis neglects the body force associated with gravity and the effects of gas phase radiation heat transfer. The effects of buoyancy and radiation could make stabilizing low strain rate counterflow flames in the laboratory very challenging. An alternative environment which may include double CH concentration peaks is the partially premixed coflow jet flame. At least one previous study reported detailed species measurements in these coflow flames obtained using laser diagnostics, but CH radical was not measured [43]. Heberle et al. performed nonquantitative measurements of CH using LIF in these types of flames but did not report double peaks [53]. If this unique structure were found in coflow jet flames, the unusual $EINO_x$ behavior of these flames reported in Refs. 14–17 might become better understood.

SUMMARY AND CONCLUSIONS

Partially premixed flames with low strain rates were stabilized computationally using the Oppdif counterflow flame code with radial velocity gradients imposed at the fuel and air nozzles. Under these conditions, a unique flame structure which affects NO formation and destruction exists. Above $\Phi_B = 2.5$, the present flame structure is described as a CH_4/air premixed flame merged with a CO/H_2/air nonpremixed flame. Below $\Phi_B = 2.5$, the two flame zones exist on opposite sides of the stagnation plane, and the CO/H_2/air nonpremixed flame is characterized by hydrocarbon concentration peaks on its fuel-side edge. Thus, the flames with Φ_B below 2.5 contain two CH radical concentration peaks, one at the location of the CH_4/air premixed flame and one at the fuel-side edge of the CO/H_2/air nonpremixed flame. The CH_2 and CH_3 species also exhibit double peaked behavior. One of the double hydrocarbon concentration peaks "belongs" to the CH_4/air premixed flame, while the other "belongs" to the CO/H_2/air nonpremixed flame. This flame structure exists because CH_4, CH_3, and CH_2 survive the CH_4/air premixed flame and react at the edge of the oxygen consumption zone associated with the CO/H_2/air nonpremixed flame.

There are several significant findings of the present study concerning NO behavior in low strain rate counterflow flames which exhibit the structure described in this paper. First, in the flames with two CH concentration peaks, NO is produced in one or more formation zones, and then transported into a destruction zone which overlaps only partially with the formation zone. Here, the NO is consumed by CH_i + NO reactions and by the HCCO + NO reaction. Of the CH_i species, CH_2 consumes NO most rapidly. The flames with double CH peaks exhibit (1) an NO destruction zone which *begins* on the reactant side of the CH_4/air premixed flame and

persists throughout the broad region *between* the two CH peaks, (2) an NO formation zone on the air side of the CO/H_2/air nonpremixed flame CH peak, and (3) an NO formation zone near the CO/H_2/air nonpremixed flame temperature peak. Even though there is a change in the flame structure at $\Phi_B = 2.5$ which affects the character of the CH_i + NO reburn zones, there is no noticeable change in the importance of NO destruction reactions relative to formation reactions at this equivalence ratio. In fact, the importance of NO destruction relative to NO formation increases uniformly as Φ_B increases. Finally, the fuel-side equivalence ratio is the most important indicator of how much NO is destroyed relative to how much is formed in low strain rate partially premixed flames, and NO destruction reactions are more important in pure diffusion flames than in partially premixed flames for low strain rate conditions.

It is likely that a flame with multiple strain rates, such as a coflow partially premixed jet flame, will exhibit regions in which the NO formation is similar to that computed for high strain rate flames in Refs. 28 and 31 and regions in which the NO formation is similar to that computed for low strain rate flames in the present study. The net effect of this complex strain rate environment is the global exhaust $EINO_x$ minimum reported in Refs. 14–16. To the authors' knowledge, the present computed low strain rate flame structure has not been identified experimentally, which is probably a result of the difficulty of stabilizing low strain rate flames. The discovery of this structure in laboratory flames might provide insight into the unusual $EINO_x$ behavior of partially premixed flames. It is hoped that the present results will provide motivation for future researchers to search for this structure in laboratory flames.

Financial support for this work was provided by the National Science Foundation Grant No. CTS-915720, by the Office of Naval Research Grant No. N00014-94-0624, and by a Clare Boothe Luce graduate fellowship administered by Purdue University for the Henry Luce Foundation. The authors thank Dr. Andrew Lutz for his guidance and patience in helping them use Oppdif. Professor Normand Laurendeau, Dr. William Pitts, and Dr. John Hewson are acknowledged for their helpful suggestions.

REFERENCES

1. Blevins, L. G., and Gore, J. P., *Combust. Sci. Technol.* 109:255 (1995).
2. Fric, T. F., *J. Propul. Power* 9:708 (1993).
3. Yamaoka, I., and Tsuji, H., *Seventeenth Symposium (International) on Combustion*, The Combustion Institute, Pittsburgh, 1979, p. 843.
4. Yamaoka, I., and Tsuji, H., *Sixteenth Symposium (International) on Combustion*, The Combustion Institute, Pittsburgh, 1977, p. 1145.
5. Yamoaka, I., and Tsuji, H., *Fifteenth Symposium (International) on Combustion*, The Combustion Institute, Pittsburgh, 1975, p. 637.
6. Hamins, A., Thridandam, H., and Seshadri, K., *Chem. Eng. Sci.* 40:2027 (1985).
7. Kioni, P. N., Rogg, B., Bray, K. N. C., and Linan, A., *Combust. Flame* 95:276 (1993).
8. Ishikawa, N., *Combust. Sci. Technol.* 30:311 (1983).
9. Feng, C. C., Lam, S. H., and Glassman, I., *Combust. Sci. Technol.* 10:59 (1975).
10. Karim, G. A., and Tsang, P., *J. Fluids Eng.* 97:615 (1975).
11. Liebman, I., Corry, J., and Perlee, H. E., *Combust. Sci. Technol.* 2:365 (1971).
12. Phillips, H., *Tenth Symposium (International) on Combustion*, The Combustion Institute, Pittsburgh, 1965, p. 1277.
13. Turns, S. R., *Introduction to Combustion*, McGraw-Hill, New York 1996, p. 211.
14. Gore, J. P., and Zhan, N. J., *Combust. Flame* 105:414 (1996).
15. Kim, T. K., Alder, B. J., Laurendeau, N. M., and Gore, J. P., *Combust. Sci. Technol.* 110:361 (1995).
16. Lyle, K. H. (1997). M.S. thesis, Purdue University.
17. Li, S. C., Ilincic, N., and Williams, F. A., *J. Eng. Gas Turbines Power* 119:836 (1997).
18. Driscoll, J. F., Chen, R. H., and Yoon, Y., *Combust. Flame* 88:37 (1992).
19. Turns, S. R., Myhr, F. H., Bandaru, R. V., and Maund, E. R., *Combust. Flame* 93:255 (1993).
20. Rokke, N. A., Hustad, J. E., and Sonju, O. K., *Combust. Flame* 97:88 (1994).
21. Smyth, K. C., *Combust. Sci. Technol.* 115:151 (1996).
22. Bowman, C. T., Hanson, R. K., Davidson, D. F., Gardiner, Jr., W. C., Lissianski, V., Smith, G. P., Golden, D. M., Frenklach, M., and Goldenberg, M., http://www.me.berkeley.edu/gri_mech, 1996.
23. Hahn, W. A., and Wendt, J. O. L., *Eighteenth Symposium (International) on Combustion*, The Combustion Institute, Pittsburgh, 1981, p. 121.
24. Dixon-Lewis, G., David, T., Gaskell, P. H., Fukutani, S., Jinno, H., Miller, J. A., Kee, R. J., Smooke, M. D., Peters, M. D., Effelsberg, E., Warnatz, J., and Behrendt, F., *Twentieth Symposium (International) on Combustion*, The Combustion Institute, Pittsburgh, 1985, p. 1893.

25. Kee, R. J., Miller, J. A., Evans, G. H., and Dixon-Lewis, G., *Twenty-Second Symposium (International) on Combustion*, The Combustion Institute, Pittsburgh, 1988, p. 1479.
26. Dixon-Lewis, G., *Twenty-Third Symposium (International) on Combustion*, The Combustion Institute, Pittsburgh, 1990, p. 305.
27. Lutz, A. E., and Kee, R. J. (1996) *A FORTRAN Program for Computing Opposed-Flow Diffusion Flames*, Sandia National Laboratories Rept. No. SAND96-8243.
28. Nishioka, M., Nakagawa, S., Ishikawa, Y., and Takeno, T., *Combust. Flame* 98:127 (1994).
29. Dupont, V., Pourkashanian, M., Richardson, A. P., Williams, A., and Scott, M. J., *Transport Phenomena in Combustion, Volume 1*, Taylor and Francis, New York, 1996, p. 263–274.
30. Miller, J. A., and Bowman, C. T., *Prog. Energy Combust. Sci.* 15:287 (1989).
31. Tanoff, M. A., Smooke, M. D., Osborne, R. J., Brown, T. M., and Pitz, R. W., *Twenty-Sixth Symposium (International) on Combustion*, The Combustion Institute, Pittsburgh, 1996, p. 1121.
32. Blevins, L. G. (1996). Ph.D. thesis, Purdue University.
33. Kee, R. J., Dixon-Lewis, G., Warnatz, J., Coltrin, M. E., and Miller, J. A. (1986). *A Fortran Computer Code Package for the Evaluation of Gas-Phase Multicomponent Transport Properties*, Sandia National Laboratories Rept. SAND86-8246.
34. Oran, E. S., and Boris, J. P., *Prog. Energy Combust. Sci.* 7:1 (1981).
35. Kee, R. J., Rupley, F. M., and Miller, J. A. (1989). *Chemkin-II: A Fortran Chemical Kinetics Package for the Analysis of Gas-Phase Chemical Kinetics*, Sandia National Laboratories Rept. SAND89-8009B.
36. Grcar, J. F., Kee, R. J., Smooke, M. D., and Miller, J. A., *Twenty-First Symposium (International) on Combustion*, The Combustion Institute, Pittsburgh, 1986, p. 1773.
37. Takeno, T., and Nishioka, M., *Combust. Flame* 92:465 (1993).
38. Law, C. K., *Twenty-Second (International) Symposium on Combustion*, The Combustion Institute, 1988, p. 1381.
39. Chelliah, H. K., Law, C. K., Ueda, T., Smooke, M. D., and Williams, F. A., *Twenty-Third Symposium (International) on Combustion*, The Combustion Institute, Pittsburgh, 1990, p. 503.
40. Tsuji, H., *Prog. Energy Combust. Sci.* 8:93 (1982).
41. Bloor, M. I. G., David, T., Dixon-Lewis, G., and Gaskell, P. H., *Twenty-First Symposium (International) on Combustion*, The Combustion Institute, Pittsburgh, 1986, p. 1501.
42. Drake, M. C., and Blint, R. J., *Combust. Sci. Technol.* 61:187 (1988).
43. Nguyen, Q. V., Dibble, R. W., Carter, C. D., Fiechtner, G. J., and Barlow, R. S., *Combust. Flame* 105:499 (1996).
44. Turns, S. R. *Introduction to Combustion*, McGraw-Hill, New York, 1996, p. 236.
45. Bilger, R. W., *Combust. Flame* 30:277 (1977).
46. Norton, T. S., Smyth, K. C., Miller, J. H., and Smooke, M. D., *Combust. Sci. Technol.* 90:1 (1993).
47. Peters, N., *Ber. Bunsenges. Phys. Chem*, 87:989 (1983).
48. Nishioka, M., Kondoh, Y., and Takeno, T., *Twenty-Sixth Symposium (International) on Combustion*, The Combustion Institute, Pittsburgh, 1996, p. 2139.
49. Kilpinen, P., Glarborg, P., and Hupa, M., *Ind. Eng. Chem. Res.* 31:1477 (1992).
50. Wendt, J. O. L., Sternling, C. V., and Matovich, M. A., *Fourteenth Symposium (International) on Combustion*, The Combustion Institute, Pittsburgh, 1973, p. 897.
51. Chen, S. L., McCarthy, J. M., Clark, W. D., Heap, M. P., Seeker, W. R., and Pershing, D. W., *Twenty-First Symposium (International) on Combustion*, The Combustion Institute, Pittsburgh, 1986, p. 1159.
52. Hewson, J. C., and Bollig, M., *Twenty-Sixth Symposium (International) on Combustion*, The Combustion Institute, Pittsburgh, 1996, p. 2171.
53. Heberle, N. H., Smith, G. P., Jeffries, J. B., Crosley, D. R., Rumminger, M., and Dibble, R. W., *Proceedings of the Western States Section of the Combustion Institute*, 1990.

Received 27 October 1997; accepted 7 April 1998